

Depth-Aware Multi-Grid Deep Homography Estimation with Contextual Correlation

Lang Nie, Chunyu Lin, *Member, IEEE*, Kang Liao, *Student Member, IEEE*, Shuaicheng Liu, *Member, IEEE*, Yao Zhao, *Senior Member, IEEE*

Abstract—Homography estimation is an important task in computer vision applications, such as image stitching, video stabilization, and camera calibration. Traditional homography estimation methods heavily depend on the quantity and distribution of feature correspondences, leading to poor robustness in low-texture scenes. The learning solutions, on the contrary, try to learn robust deep features but demonstrate unsatisfying performance in the scenes with low overlap rates. In this paper, we address these two problems simultaneously by designing a contextual correlation layer (CCL). The CCL can efficiently capture the long-range correlation within feature maps and can be flexibly used in a learning framework. In addition, considering that a single homography can not represent the complex spatial transformation in depth-varying images with parallax, we propose to predict multi-grid homography from global to local. Moreover, we equip our network with a depth perception capability, by introducing a novel depth-aware shape-preserved loss. Extensive experiments demonstrate the superiority of our method over state-of-the-art solutions in the synthetic benchmark dataset and real-world dataset. The codes and models will be available at <https://github.com/nie-lang/Multi-Grid-Deep-Homography>.

Index Terms—Homography estimation, mesh deformation

I. INTRODUCTION

A homography is an invertible mapping from one image plane to another with 8-DOF, including 2 for translation, 2 for rotation, 2 for scale, and 2 for lines at infinity. It has been widely served as an essential component of various computer vision applications, such as image stitching [1], [2], video stabilization [3]–[5], camera calibration [6], and simultaneous localization and mapping (SLAM) [7].

Traditional algorithms estimate the homography in two ways. Pixel-based approaches update the homography parameters by optimizing the pixel-level alignment error between two images in an iterative way [8], often failing to deal with scenes with low overlap rates. Feature-based approaches search for the optimal homography model based on sparse feature correspondences using different feature extractors [9]–[12] and different robust estimation strategies [13]–[15]. However, they heavily depend on the number and distribution of feature

This work was supported by the National Natural Science Foundation of China (No.62172032). (*Corresponding author: Chunyu Lin*)

Lang Nie, Chunyu Lin, Kang Liao, Yao Zhao are with the Institute of Information Science, Beijing Jiaotong University, Beijing 100044, China, and also with the Beijing Key Laboratory of Advanced Information Science and Network Technology, Beijing 100044, China (email: nielang@bjtu.edu.cn, cylin@bjtu.edu.cn, kang_liao@bjtu.edu.cn, yzhao@bjtu.edu.cn).

Shuaicheng Liu is with School of Information and Communication Engineering, University of Electronic Science and Technology of China, Chengdu, 611731, China (liushuaicheng@uestc.edu.cn).

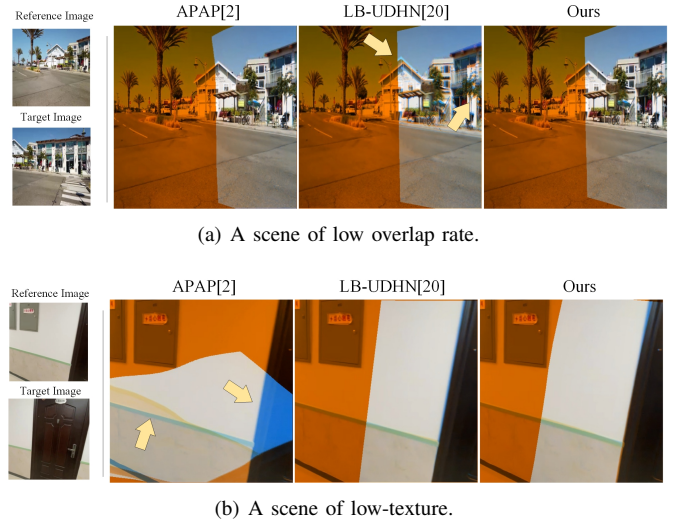


Fig. 1. Limitations of the existing solutions. The target image is warped to align with the reference image using the estimated homography. We fuse the reference image and the warped target image by setting the intensity of the blue channel in the reference image and that of the red channel in the warped target image to zero. **In this manner, the non-overlapping regions are distinguished in orange, which also implies the overlap rate. Overlapping regions (non-orange regions) are where we should focus, and the misalignments are highlighted in different colors.** The arrow points to the poorly aligned areas. The proposed method overcomes the two challenging cases by introducing the CCL — a more efficient feature matching module than the cost volume.

correspondences, leading to poor robustness in low-texture scenes.

Contrast to traditional algorithms, learning-based solutions [16]–[20] are proposed to handle the challenging low-texture scenes for their robust deep feature extraction. However, it is not efficient to explore the matching relationship between the deep feature maps by simply stacking convolutional layers. Therefore, deep learning solutions often demonstrate unsatisfying performance in scenes with low overlap rates. As shown in Fig. 1 (a), noticeable misalignments can be found in the result of the existing deep homography solution [20] when the overlap rate is low.

In addition, with a single estimated homography, neither traditional solutions nor deep learning ones can perfectly align images with parallax caused by different depth planes and different baselines. To address this limitation, non-linear multi-homography estimation algorithms [2], [21]–[23] are proposed to handle the challenging parallax. Usually, these methods partition an image into dense grids, and a distinct homography can be estimated for each grid using sparse fea-

ture correspondences. However, these multi-grid methods have higher requirements on the quantity and distribution of feature correspondences. They tend to show worse performance than single homography models in low-texture or low-resolution scenes. As shown in Fig. 1 (b), the existing traditional solution [2] fails in a low-texture indoor case.

To simultaneously overcome the problems of poor robustness for traditional algorithms in low-texture scenes and failures for deep learning algorithms in low overlap rate cases, we design a contextual correlation layer (CCL) to explicitly capture the matching relationship between deep feature maps. The proposed layer is a flexible module that can be easily embedded in other matching-related networks, making a deep learning framework robust in both low-texture and low overlap rate scenarios. Compared with the cost volume [24], [25], the proposed CCL has advantages of higher accuracy, faster speed, and lower memory consumption in the field of deep homography. Besides, to break the limitation that a single homography can not align images with parallax, we propose a multi-grid deep homography network to estimate multi-grid homography from global to local in an end-to-end framework. Specifically, the proposed network predicts a global homography first to align images coarsely and obtain the original shape of a mesh. Then the residual mesh deformation is estimated to enable our network to align images with parallax.

The proposed framework can be easily trained in an unsupervised manner using a pixel-level content alignment loss. However, a content constraint alone tends to cause unnatural deformations to the mesh, such as self-intersection. Existing methods [26], [27] handle this problem by adding a shape-preserved constraint, encouraging all grids in the mesh to be rectangular and adjacent grids to have similar shapes. Nevertheless, this measure is essentially a trade-off between content alignment and the natural mesh shape. In this paper, we rethink this trade-off from the perspective of parallax. A depth-aware shape-preserved loss is proposed to promote the content alignment and the natural mesh shape simultaneously. Formally, we assign different depth levels to all grids, and only grids at the same depth level will be enforced to keep the shape consistent. As for the grids at different depth levels, there will be no shape constraint, encouraging the content alignment as much as possible.

Extensive experiments demonstrate that our algorithm surpasses the state-of-the-art homography estimation methods in both the synthetic benchmark dataset and the real-world dataset. Moreover, a comprehensive comparison between the proposed CCL and the cost volume is provided to support our superiority.

To sum up, we conclude our contributions as follows:

- We design a novel contextual correlation layer (CCL) to explicitly explore the long-range feature correlation. It outperforms the traditional cost volume in the accuracy, the number of parameters, and the speed in the field of deep homography.
- We propose an end-to-end multi-grid homography estimation network, enabling our network to align images with parallax.

- To avoid the trade-off between the alignment and the shape, a depth-aware shape-preserved loss is presented to improve the content alignment and the natural mesh shape simultaneously.

II. RELATED WORK

A. Linear Homography Estimation

Pixel-based solutions iteratively estimate an optimal homography to minimize the alignment error, such as L1 norm, L2 norm, and negative of normalized correlation [8]. But it is challenging to handle scenarios with low overlap rates.

Different from pixel-based solutions, feature-based approaches estimate a homography by minimizing the reprojection error based on the sparse feature correspondences. The first step of these approaches is to detect sparse feature points using feature point extractors, such as SIFT [9], ORB [10], BRISK [11], and SOSNet [12]. After feature matching, a robust estimation algorithm with outliers rejection will be adopted to solve for the homography from feature correspondences, such as RANSAC [13], MAGSAC [14], and MAGSAC++ [15]. Feature-based solutions work well in scenes with low overlap rates. Still, their performance heavily depends on the quality of feature correspondences, often failing in low-texture, low-light, or low-resolution scenes.

Compared with feature-based approaches, learning-based solutions address the challenge of low-texture scenes for their robust feature extraction capability. DeTone *et al.* [16] apply deep learning to homography estimation for the first time, developing a VGG-style homography regression network. In their seminal work, the network predicts the 8 motions of the 4 vertices instead of solving the homography directly. By applying Spatial Transformer Network (STN) [28] to the homography network, Nguyen *et al.* [17] propose to train the regression network using a pixel-level photometric loss in an unsupervised manner. Zhang *et al.* [18] and Le *et al.* [29] propose to reject the foreground and dynamic objects by learning a content-aware attention mask. Chang *et al.* [30] design a cascaded Lucas-Kanade network to progressively refine the estimated homography in multi-scale deep features. To solve the problem of inefficient feature matching by convolution, Nie *et al.* [19] connect the feature pyramid and the cost volume to regress the residual homography. Although the cost volume has significantly improved the network's receptive field, the memory and time consumption have increased significantly.

In this paper, the proposed CCL can serve as a better alternative to the cost volume in the deep homography estimation with improved accuracy and reduced computational complexity.

B. Non-Linear Multi-Homography Estimation

The traditional multi-homography estimations pursue precise local alignment in the overlapping regions. Zaragoza *et al.* [2] propose to place a mesh on the image domain and compute a local homography for every grid to achieve as-projective-as-possible (APAP) warp. To get more natural-looking results with less projective distortions, Lin *et al.* [21] refine the local warp by connecting the homography model with similarity

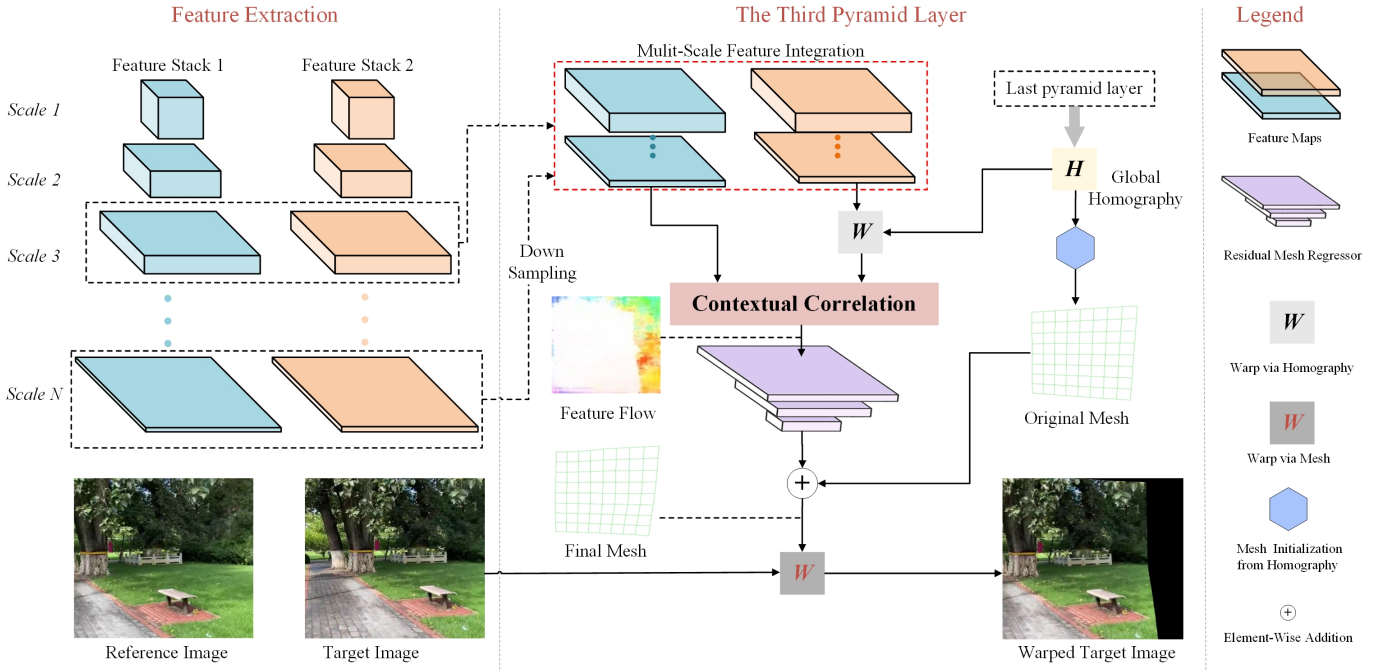


Fig. 2. An overview of the proposed multi-grid deep homography network. The estimation can be done in a three-layer pyramid, where the first two layers predict the global homography and the third one predicts local multi-grid homography. The architecture of the third layer is demonstrated in the middle of the figure, where the multi-grid homography can be represented as the mesh.

transformation. To get better alignment performance, Li *et al.* [31] propose a robust elastic warping (robust ELA) that can be regarded as a combination of the grid-based model and the direct deformation strategy. In [32], Liao and Li propose two single-perspective warps to preserve perspective consistency with reduced projective distortions. Lee *et al.* [22] partition an image into superpixels and warp them adaptively according to an optimal homography computed from the warping residual vectors. Also, Jia *et al.* [33] leverage the line-point consistency constraint to preserve structures for wide parallax image stitching.

These traditional multi-homography solutions can achieve better alignment results than single homography solutions, especially in scenes with parallax. However, to calculate distinct local warps accurately, they have stricter requirements on the quality of feature points, often performing worse than single homography solutions in low-texture or low-resolution scenarios.

The existing learning-based multi-homography solutions are related to video stabilization, which can be seen as a small-baseline alignment application. Wang *et al.* [26] propose to learn a multi-grid transformation network to align adjacent video frames. To train this network stably, the inter-grid consistency term and intra-grid regularity term are adopted to maintain the shape of the grids. In [34], a deep learning alternative of MeshFlow [5] is presented, which is content-aware and can reject dynamic objects in small-baseline scenes. These methods eliminate the dependence on the feature points and demonstrate significantly improved robustness in low-texture scenes.

However, in applications of low overlap rates such as image stitching, these learning frameworks are not robust or even

can not work. In contrast, the proposed network can solve this problem well.

III. METHODOLOGY

A. Network Overview

The proposed algorithm is a learning-based multi-grid deep homography solution, whose architecture is shown in Fig. 2. Given a reference image I_r and a target image I_t , we aim to regress the multi-grid homography that can warp the target image to align with the reference image. Following the previous works [16], [17], we represent the homography as eight motions of the four vertices which can be formulated as a matrix of size $2 \times 2 \times 2$. Then, the $U \times V$ multi-grid homography can be represented as a matrix of size $(U + 1) \times (V + 1) \times 2$.

We adopt a series of convolution-pooling blocks with shared weights to extract deep features ($F_r^k, F_t^k, k = 1, 2, \dots, N$) of the input images at different scales. Then we resize and stack these features of different scales to formulate a feature pyramid, where the l -th layer integrates the multi-scale features from scale l to scale N . Next, we use the top part of the feature pyramid ($l = 1, 2, 3$) to predict the multi-grid homography from the integrated multi-scale features. In our design, the l -th layer takes the predicted homography from the $(l - 1)$ -th layer as the known prior information of the current layer and predicts the residual homography. Specifically, the first two pyramid layers predict the global homography while the third pyramid layer predicts the $U \times V$ multi-grid homography. In this way, we predict the multi-grid homography from global to local, enabling our network to process images with parallax.

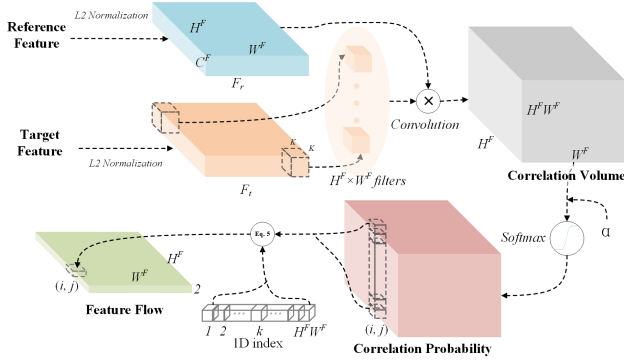


Fig. 3. The structure of the proposed CCL. Step 1: Calculate the correlation volume by the convolution operation. Step 2: Convert the correlation volume into correlation probability. Step 3: Compute the final feature flow through Eq. (5).

B. Contextual Correlation

The existing deep homography solutions do not work well in scenes with low overlap rates because the convolutional layers can not explore the long-range correlation efficiently. To solve this problem, Nie *et al.* [19] introduce the cost volume into the network to explicitly enhance the feature matching capability. However, the application of the cost volume significantly increases the cost of space and time. To alleviate this problem, we propose the CCL, whose structure is shown in Fig. 3. It takes the feature maps of I_r , I_t as input and outputs a dense feature flow. We define the feature flow as the motions of feature correspondences that contain the vertical and horizontal movements.

Compared with the cost volume, the proposed module has the following advantages: (1) better performance in deep homography, (2) faster speed, (3) less memory consumption, (4) more robust on correlation matching thanks to patch-to-patch matching instead of point-to-point matching. The first three advantages will be proved in the experiments of Section IV-D, and the last one will be explained in the first step of the following implementation.

Next, we introduce three steps of the implementation:

1) Correlation Volume.

We first normalize the multi-scale features (shown in the top of Fig. 2) using l_2 norm on the channel dimension as $F_r, F_t \in H^F \times W^F \times C^F$ and then extract the potential correlation relationship between them.

The cost volume [25] extracts the global correlation relationship from F_r, F_t as a 3D volume with the shape of $H^F \times W^F \times (2H^F + 1)(2W^F + 1)$, and represents the correlation in cosine similarity as follows:

$$c_{x_r, y_r, x_t, y_t} = \frac{\langle F_r^{x_r, y_r}, F_t^{x_t, y_t} \rangle}{|F_r^{x_r, y_r}| |F_t^{x_t, y_t}|}, \quad (1)$$

where (x_r, y_r) and (x_t, y_t) denote the spatial location on F_r and F_t , respectively. c is the cosine similarity between $F_r^{x_r, y_r}$ and $F_t^{x_t, y_t}$.

Compared with the cost volume that computes the point-to-point correlation, we calculate the patch-to-patch correlation between arbitrary $K \times K$ regions in this step. As shown on the top of Fig. 3, we first extract dense patches ($K \times K$) from

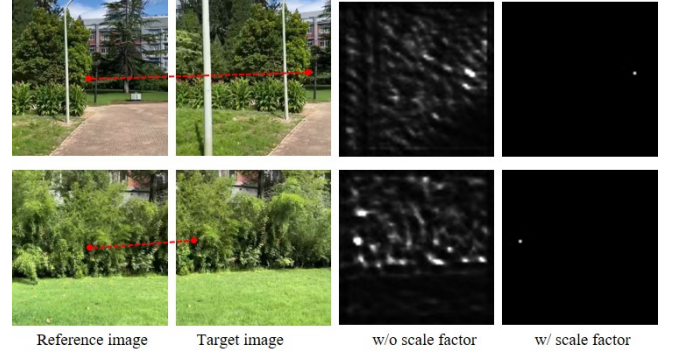


Fig. 4. The effect of the scale factor α . The red points in the reference/target image indicates the true matched points. In the visualization results of col 3-4, the whiter, the higher the correlation probability.

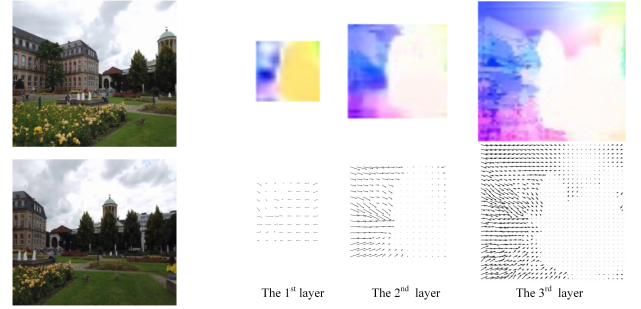


Fig. 5. The visualization of feature flows produced by the proposed CCL. (b) Top: the color representation. (b) Bottom: the motion representation. The network can predict the accurate homography or mesh only through the feature flows. To show the effect of the feature flows, The aligned result of every pyramid layer is also concluded.

F_t with the stride set to 1. Then we stack these patches as convolutional filters and use them to perform a convolutional operation on F_r . We call the output of the convolution the correlation volume whose shape is $H^F \times W^F \times H^F \times W^F$. Each value in this volume represents the similarity between a pair of arbitrary regions and can be formulated as Eq. (2):

$$c'_{x_r, y_r, x_t, y_t} = \frac{\lfloor K/2 \rfloor \langle F_r^{x_r+i, y_r+j}, F_t^{x_t+i, y_t+j} \rangle}{\sum_{i, j=-\lfloor K/2 \rfloor}^{\lfloor K/2 \rfloor} |F_r^{x_r+i, y_r+j}| |F_t^{x_t+i, y_t+j}|}, \quad (2)$$

where $\lfloor \cdot \rfloor$ represents the operation of round down. Compared with the shape of the cost volume, the shape of proposed correlation volume is only a quarter.

2) Scale Softmax.

Every position in the correlation volume can be regarded as a vector with the length of $H^F \times W^F$. We set $K = 3$ and every value in this vector ranges from 0 to 9. Then we

use the softmax function to activate these vectors, converting the feature matching into an issue of classification ($H^F W^F$ categories). In this fashion, the correlation volume is converted to the correlation probability as illustrated in the right of Fig. 3. Inspired by [35], these vectors will be multiplied by a constant scale factor α ($\alpha > 1$) before the activation to increase the between-class distance.

Let the vector of correlation volume at each location be $[x_1, x_2, \dots, x_{H^F W^F}]^T$, and suppose $x_1 \leq x_2 \leq \dots \leq x_{H^F W^F}$. Then we can get the probability of matching of x_k ($k \in \{1, 2, \dots, H^F W^F\}$) with or without scale factor α as follows:

$$p_k = \frac{e^{x_k}}{\sum_{i=1}^{H^F W^F} e^{x_i}} = \frac{1}{1 + \sum_{i=1}^{k-1} e^{x_i - x_k} + \sum_{i=k+1}^{H^F W^F} e^{x_i - x_k}}, \quad (3)$$

$$p_k^\alpha = \frac{e^{\alpha x_k}}{\sum_{i=1}^{H^F W^F} e^{\alpha x_i}} = \frac{1}{1 + \sum_{i=1}^{k-1} e^{\alpha(x_i - x_k)} + \sum_{i=k+1}^{H^F W^F} e^{\alpha(x_i - x_k)}}. \quad (4)$$

Comparing the denominator of Eq.3 with that of Eq.4, we can observe that this scale factor can make p_k with low matching probability lower (when k is far less than $H^F W^F$) and p_k with the highest matching probability higher (when $k = H^F W^F$). In other words, weak correlations are suppressed while the strongest correlation is enhanced. To further verify this view, Fig.4 visualizes the vectors at the center of the correlation volumes after softmax with or without scale factor in 2D. It can be seen that, without the scale factor, many regions in the target image domain (col 3) are similar to the center points of the reference image. In contrast, most of the mismatched regions are rejected (col 4) with this factor.

3) Feature Flow.

In this step, we rethink the essence of the deep homography estimation — regressing the 8 motions of 4 vertices in 2 orthogonal directions of the target image. Based on this comprehension, we believe that the difficulty of predicting the homography can drop if we regress the homography motions from the feature motions that indicate the dense correlations in feature maps. Hence, we propose to convert the correlation volume into feature flow — the dense feature motions between feature correspondences at the feature level.

Let $p_k^{i,j}$ represents the value of correlation volume with scale softmax activated at position (i, j, k) , the feature motion ($m_{hor}^{i,j}, m_{ver}^{i,j}$) at position (i, j) can be calculated as follows:

$$(m_{hor}^{i,j}, m_{ver}^{i,j}) = \sum_{k=1}^{H^F W^F} p_k^{i,j} (\text{mod}\{k, W^F\}, \lfloor k/W^F \rfloor) - (i, j), \quad (5)$$

where $\text{mod}\{\cdot, \cdot\}$ denotes the modulus operation.

Ultimately, we obtain the feature flow ($H^F \times W^F \times 2$) from the reference feature to the target feature as the input of the subsequent regression network. We visualize the feature flows in Fig. 5, where the intermediate feature flows and the final aligned results in every pyramid layer are displayed in pairs.

Also, a comparison of the complexity between the cost volume and our CCL is provided in Table I. Compared with the cost volume, the CCL outputs the lightweight representation of feature flows by rejecting most unmatched positions, leading to more efficient prediction.

TABLE I
COMPARISON OF COMPLEXITY BETWEEN THE COST VOLUME AND PROPOSED CONTEXTUAL CORRELATION. SUPPOSE $H^F = W^F = n$.

	Cost volume	Contextual correlation
Implementation	Loop	Convolution
Space complexity	$O(n^4)$	$O(n^4)$
Time complexity	$O(n^2)$	$O(1)$

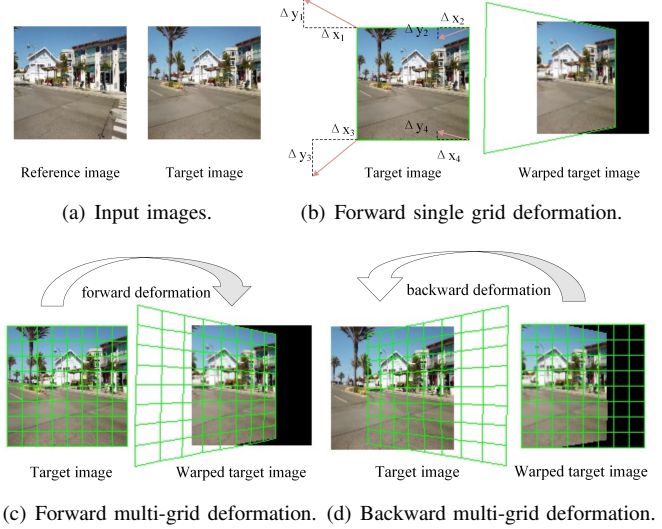


Fig. 6. Comparison between the forward deformation and backward deformation.

C. Backward Multi-Grid Deformation

The existing deep homography solutions predict the 8 motions of the 4 vertices in the target image instead of directly solving the 8 unknown parameters in the homography. With the 8 motions, we can solve for the corresponding homography and warp the target image to align with the reference image as shown in Fig. 6 (a)(b). We call this motion direction from the target image domain to the reference image domain as the forward deformation. Then, by placing a mesh on the target image, we can extend the single grid deformation (1×1) to multi-grid deformation ($U \times V$) as shown in Fig. 6 (c). Different from single grid warping in which every pixel shares the same homography, multi-grid warping has to assign a different homography to each pixel in the warped target image. In other words, in multi-grid warping, we need to figure out which grid the pixel in the warped target image belongs to. Since the mesh shape in the warped target image is irregular after the forward deformation, it is hard to obtain the correspondence between each grid and each pixel in the warped target image using a fast and efficient way in a deep learning implementation. Therefore, if we continue to adopt the forward deformation, it can drastically reduce the speed.

To avoid this problem, we design a backward deformation solution. Specifically, as shown in Fig. 6 (d), we place a regular mesh in the warped target image and then predict the grid motions from the reference image domain to the target image domain. Compared with the forward deformation, the mesh shape in the warped target image is regular in the proposed backward deformation. Therefore, we can easily

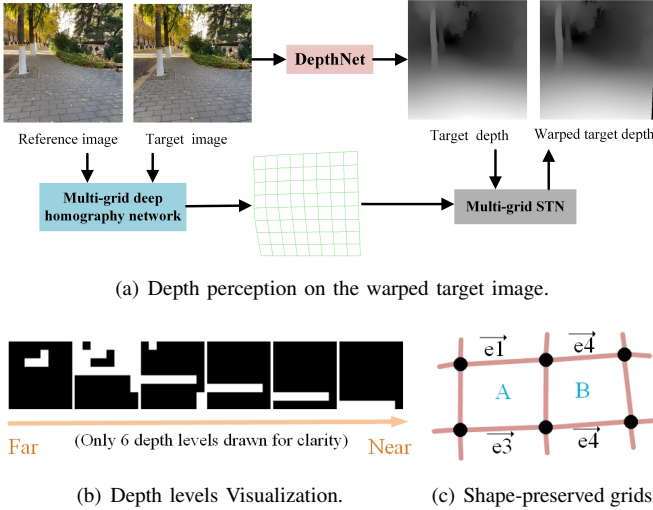


Fig. 7. Depth-aware shape-preserved loss. (a) Depth perception from a pretrained monocular depth estimation network (b) Depth levels division on the mesh. (c) The shape-preserved constraint on adjacent edges in the same depth level.

assign different homography to each pixel of the warped target image in batches, enabling parallel acceleration in GPU.

D. Unsupervised Training

The proposed multi-grid deep homography network is trained in a fully unsupervised manner since there is no ground truth in real-world scenes. In this paper, we design a content alignment term and a shape-preserved term to optimize our network. The content alignment term is adopted to align the input images in image contents, while the shape-preserved term is designed to keep the mesh shape from unnatural distortions.

1) Content Alignment Loss.

Given a reference image I_r and a target image I_t with overlapping regions, the network is expected to align the overlapping regions. Let $\mathcal{W}^k(\cdot)$ be the operation of spatial transformation using the predicted mesh in the k -th layer of the feature pyramid. Then the content alignment constraint in this layer can be written as follows:

$$L_{content}^k = \|\mathcal{W}^k(E) \odot I_r - \mathcal{W}^k(I_t)\|_1, \quad (6)$$

where E is an all-one matrix and \odot is the operation of element-wise multiplication.

Considering our network consists of 3 pyramid layers, the content alignment loss should be:

$$L_{content} = \omega_1 L_{content}^1 + \omega_2 L_{content}^2 + \omega_3 L_{content}^3, \quad (7)$$

where ω_1 , ω_2 , and ω_3 are the weights for different pyramid layers.

2) Depth-Aware Shape-Preserved Loss.

Optimizing the network using content alignment loss alone can cause unnatural mesh distortions, such as self-intersection. To avoid this problem, a shape-preserved loss is proposed in [26], [34], which encourages adjacent grids to maintain similar shapes. However, this constraint can easily spread from

adjacent grids to the surroundings, enforcing all the grids to maintain a similar shape. This manner treats all grids as being on the same plane, improving the shape regularity at the cost of reducing the content alignment performance.

In this paper, we rethink this shape-preserved loss: the ideal loss should only impose the shape-preserved constraint on grids at the same depth, but not on grids at different depths. To implement it, we design a depth-aware shape-preserved loss, which can estimate different depth levels on the mesh and constrain the grids at the same depth level to maintain similar shapes.

The process of calculating the depth-aware shape-preserved loss is shown in Fig. 7. First, we adopt a pre-trained monocular depth estimation model [36] to predict the depth map of the target image. Then, we warp the depth map using the multi-grid homography estimated from our network. Having obtained the warped depth maps, we compute the average depth value in every grid of the warped depth map. Next, we divide the warped depth map into M different levels ($D^k, k = 1, 2, \dots, M$) with the same intervals. The depth levels are visualized in Fig. 7 (b), where the white indicates these regions are at the same depth.

Assuming all the grids are at the same depth level, we can warp them with the same homography, and each line in the deformed mesh is a straight line. Based on this observation, we constrain the direction of grid edge consistent in adjacent grids at the same depth. An example is shown in Fig. 7 (c), where the similarity between grid A and B can be formulated as follows:

$$t_{sp}^{A,B} = 2 - \frac{|\vec{e}_1 \cdot \vec{e}_2|}{\|\vec{e}_1\| \cdot \|\vec{e}_2\|} - \frac{|\vec{e}_3 \cdot \vec{e}_4|}{\|\vec{e}_3\| \cdot \|\vec{e}_4\|}. \quad (8)$$

According to Eq. (8), we can calculate the similarity matrices (L_{sp}^{hor} and L_{sp}^{ver}) on horizontal and vertical directions of the deformed mesh, where the sizes of L_{sp}^{hor} and L_{sp}^{ver} are $U \times (V - 1)$ and $(U - 1) \times V$, respectively. Finally, we formulate our depth-aware shape-preserved loss as follows:

$$L_{shape} = \frac{1}{U(V-1)} \sum_{k=1}^M D_{hor}^k L_{sp}^{hor} + \frac{1}{(U-1)V} \sum_{k=1}^M D_{ver}^k L_{sp}^{ver}, \quad (9)$$

where D_{hor}^k and D_{ver}^k are depth consistency matrices on the horizontal and vertical directions, and they are calculated from D^k . Every element in D_{hor}^k ($U \times (V - 1)$) and D_{ver}^k ($(U - 1) \times V$) indicates if the adjacent grids (horizontal direction or vertical direction) are at the same depth level.

3) Objective Function.

Taking the content alignment term and shape-preserved term into consideration simultaneously, we conclude the objective function of our network:

$$L = \lambda L_{content} + \mu L_{shape}, \quad (10)$$

where λ and μ are the weights of $L_{content}$ and L_{shape} , respectively.

TABLE II
COMPARISON EXPERIMENT ON WARPED MS-COCO [16]. THE 1ST AND 2ND BEST SOLUTIONS ARE MARKED IN RED AND BLUE, RESPECTIVELY.

	4-pt Homography RMSE (\downarrow)			
	Easy	Moderate	Hard	Average
$I_{3\times 3}$	15.0154	18.2515	21.3548	18.5220
SIFT [9]+RANSAC [13]	0.6687	1.1223	18.5990	7.9769
ORB [10]+RANSAC [13]	3.8995	10.2206	<i>F</i>	<i>F</i>
BRISK [11]+RANSAC [13]	1.2179	2.6831	<i>F</i>	<i>F</i>
SOSNet [12]+RANSAC [13]	0.6228	1.0162	15.7217	6.7804
SIFT [9]+MAGSAC [14]	0.5697	0.8679	<i>F</i>	<i>F</i>
ORB [10]+MAGSAC [14]	3.1557	8.7443	<i>F</i>	<i>F</i>
BRISK [11]+MAGSAC [14]	1.1472	2.6300	<i>F</i>	<i>F</i>
SOSNet [12]+MAGSAC [14]	0.5790	0.9006	<i>F</i>	<i>F</i>
SIFT [9]+MAGSAC++ [15]	0.5663	0.8388	<i>F</i>	<i>F</i>
ORB [10]+MAGSAC++ [15]	2.7802	7.7074	<i>F</i>	<i>F</i>
BRISK [11]+MAGSAC++ [15]	1.0144	2.2898	<i>F</i>	<i>F</i>
SOSNet [12]+MAGSAC++ [15]	0.5564	0.8139	<i>F</i>	<i>F</i>
DHN [16]	3.2998	4.8839	7.7017	5.5358
UDHN [17]	2.1894	3.5272	6.5073	4.3179
CA-DHN [18]	15.0082	18.2498	<i>F</i>	<i>F</i>
LB-DHN [19]	0.2719	0.4140	0.9761	0.5962
LB-UDHN [20]	1.1773	1.4544	3.0702	2.0239
Ours	0.2163	0.3349	0.7076	0.4484

IV. EXPERIMENTAL RESULTS

A. Datasets and Implement Details

Datasets. We validate the performance of the proposed network in two public datasets. The first one is a synthetic benchmark dataset that is called Warped MS-COCO [16]. The samples in this dataset are image pairs without parallax, thus the target image can be aligned with the reference image perfectly using a single homography. The second dataset is a real-world dataset that is proposed in an unsupervised deep image stitching work [20], where 10,440 image pairs are used for training and 1,106 image pairs are used for testing. This dataset, called UDIS-D, consists of varying overlap rates, different degrees of parallax, and variable scenes such as indoor, outdoor, night, dark, snow, and zooming.

Implement Details. Our network is trained using an Adam [37] optimizer with an exponentially decaying learning rate initialized to 10^{-4} for 500k iterations. The batch size is set to 4, and we first train the network for 300k iterations with λ and μ set to 1 and 0, respectively. For the remaining 200k iterations, we set λ and μ to 1 and 10. And ω_1 , ω_2 , ω_3 and α are assigned as 1, 4, 16, and 10. We use RELU as the activation function for all the convolutional layers except that the last layer in the regression network adopts no activation function. The implementation is based on TensorFlow and the network is performed on a single GPU with NVIDIA RTX 2080 Ti. It takes about 96ms to align the images of 512×512 resolution.

B. Comparison on Synthetic Benchmark Dataset

Since Warped MS-COCO is a synthetic dataset without parallax, we only compare our solution with other single homography solutions. Besides, we modify the third pyramid level of the regression network to predict a single homography instead of the multi-homography for fairness. We train our

network in a supervised manner because of the availability of the ground truth.

We first compare ours with traditional feature-based solutions. As shown in Table II, we choose various feature descriptors, *e.g.* SIFT [9], ORB [10], BRISK [11] and SOSNet [12], and different outliers rejection algorithms, *e.g.* RANSAC [13], MAGSAC [14], MAGSAC++ [15], composing 12 distinct solutions. Of these feature descriptors, SOSNet is adopted to replace the local descriptors of SIFT with deep learning features.

Then we compare ours with deep learning-based solutions, *e.g.* DHN [16], UDHN [17], CA-DHN [18], LB-DHN [19] and LB-UDHN [20]. All the learning solutions including ours are trained in this dataset.

We adopt 4-pt homography RMSE from [17], [20] as the metric to evaluate all the above solutions. Formally, we divide the testing results into 3 levels according to the performance — easy (top 0-30%), moderate (top 30-60%), and hard (top 60-100%). $I_{3\times 3}$ refers to a 3×3 identity matrix as a “no-warping” homography for the reference.

The results are shown in Table II, where *F* indicates the performance of the solution is worse than that of $I_{3\times 3}$. Observed from this table, it is evident to conclude that:

(1) Our network outperforms other solutions, including traditional and deep learning algorithms in all cases (“easy”, “moderate”, and “hard”).

(2) The deep learning solutions are more robust since they are superior to traditional solutions in “hard” columns. This advantage benefits from the robust feature extraction ability of CNNs.

In the experiment, we do not compare ours with [30], [38] because they are essentially template matching algorithms. Specifically, they will take a big reference image and a small template image as inputs in these methods, where the overlap rates between the inputs can be 100%. In contrast, these compared methods and ours deal with inputs with a relatively low overlap rate.

C. Comparison on Real-World Dataset

Quantitative Comparison.

The real-world image pairs that contain rich depth levels are captured under different camera baselines, which indicates they can not be aligned using a single homography due to the parallax. Therefore, in this real-world dataset (UDIS-D), we add a comparison with the multi-homography solutions — APAP [2], AANAP [21], robust ELA [31], SPW [32] and LCP [33]. Since the mesh in our network is 8×8 (the reason for adopting 8×8 mesh in our network will be explained in Section IV-E), it is fair to compare ours with these methods that set the mesh to 8×8 . To further highlight our performance, we also compare them with the mesh set to 100×100 .

In addition, we carry on the experiments in UDIS-D in two different resolutions as shown in Table III. Formally, the resolution of images in UDIS-D is 512×512 , we resize them to 128×128 to get a low-resolution version for two reasons: 1) The low-resolution images can simulate the challenging scenes with fewer feature points. 2) Most existing deep learning

TABLE III
 QUANTITATIVE COMPARISON WITH STATE-OF-THE-ARTS ON REAL-WORLD DATASET (UDIS-D). THE 1ST AND 2ND BEST SOLUTIONS ARE MARKED IN RED AND BLUE, RESPECTIVELY.

(a) Quantitative comparison on low-resolution.

	128 × 128							
	PSNR (↑)				SSIM (↑)			
	Easy	Moderate	Hard	Average	Easy	Moderate	Hard	Average
$I_{3 \times 3}$	16.19	13.05	10.87	13.12	0.397	0.173	0.065	0.197
SIFT [9]+RANSAC [13]	25.23	22.23	17.53	21.25	0.860	0.766	0.558	0.711
ORB [10]+RANSAC [13]	21.94	18.58	13.49	17.55	0.734	0.575	0.361	0.537
BRISK [11]+RANSAC [13]	24.38	21.53	16.14	20.23	0.832	0.735	0.502	0.671
SOSNet [12]+RANSAC [13]	25.35	22.17	17.37	21.20	0.859	0.766	0.549	0.707
SIFT [9]+MAGSAC [14]	25.51	22.21	17.14	21.17	0.868	0.767	0.544	0.708
ORB [10]+MAGSAC [14]	22.33	18.56	13.71	17.75	0.754	0.587	0.369	0.550
BRISK [11]+MAGSAC [14]	24.18	21.04	16.04	19.98	0.822	0.714	0.498	0.660
SOSNet [12]+MAGSAC [14]	25.42	21.75	16.10	20.59	0.864	0.747	0.495	0.681
SIFT [9]+MAGSAC++ [15]	25.64	22.32	17.01	21.19	0.870	0.772	0.539	0.708
ORB [10]+MAGSAC++ [15]	22.36	18.86	13.56	17.79	0.755	0.595	0.370	0.553
BRISK [11]+MAGSAC++ [15]	24.63	21.41	16.17	20.28	0.839	0.730	0.501	0.671
SOSNet [12]+MAGSAC++ [15]	25.59	21.98	16.15	20.72	0.869	0.761	0.499	0.689
DHN [16]	16.40	13.36	11.48	13.52	0.409	0.170	0.076	0.204
UDHN [17]	19.39	15.93	13.09	15.83	0.573	0.334	0.165	0.338
CA-DHN [18]	<i>F</i>	13.13	11.00	13.16	0.339	0.181	0.105	0.198
LB-DHN [19]	24.75	21.14	18.43	21.14	0.825	0.712	0.547	0.680
LB-UDHN [20]	27.84	23.95	20.70	23.80	0.902	0.830	0.685	0.793
Ours (8 × 8)	28.41	24.63	21.59	24.54	0.913	0.853	0.733	0.823

(b) Quantitative comparison on original resolution.

	512 × 512							
	PSNR (↑)				SSIM (↑)			
	Easy	Moderate	Hard	Average	Easy	Moderate	Hard	Average
$I_{3 \times 3}$	15.87	12.76	10.68	12.86	0.530	0.286	0.146	0.303
SIFT [9]+RANSAC [13]	28.75	24.08	18.55	23.27	0.916	0.833	0.636	0.779
ORB [10]+RANSAC [13]	27.53	22.85	17.37	22.06	0.888	0.772	0.550	0.718
BRISK [11]+RANSAC [13]	28.57	24.02	18.63	23.23	0.911	0.824	0.629	0.772
SOSNet [12]+RANSAC [13]	28.60	23.85	17.47	22.71	0.915	0.824	0.596	0.760
SIFT [9]+MAGSAC [14]	27.42	22.39	17.07	21.77	0.891	0.777	0.574	0.730
ORB [10]+MAGSAC [14]	26.36	21.49	16.26	20.86	0.867	0.729	0.516	0.685
BRISK [11]+MAGSAC [14]	26.28	20.82	16.25	20.63	0.868	0.710	0.504	0.675
SOSNet [12]+MAGSAC [14]	26.13	19.55	14.25	19.39	0.867	0.693	0.456	0.650
SIFT [9]+MAGSAC++ [15]	27.90	22.39	17.11	21.93	0.901	0.779	0.565	0.730
ORB [10]+MAGSAC++ [15]	27.32	22.02	16.05	21.22	0.884	0.749	0.515	0.696
BRISK [11]+MAGSAC++ [15]	27.05	20.89	16.02	20.79	0.884	0.717	0.497	0.679
SOSNet [12]+MAGSAC++ [15]	26.33	19.26	13.73	19.16	0.872	0.675	0.433	0.637
DHN [16]	-	-	-	-	-	-	-	-
UDHN [17]	-	-	-	-	-	-	-	-
CA-DHN [18]	<i>F</i>	<i>F</i>	<i>F</i>	<i>F</i>	<i>F</i>	<i>F</i>	0.150	<i>F</i>
LB-DHN [19]	-	-	-	-	-	-	-	-
LB-UDHN [20]	-	-	-	-	-	-	-	-
APAP [2] (8 × 8)	27.58	23.92	19.90	23.41	0.895	0.824	0.663	0.781
AANAP [21] (8 × 8)	27.59	23.85	19.70	23.31	0.896	0.823	0.659	0.779
robust ELA [31] (8 × 8)	28.08	23.62	18.16	22.77	0.896	0.803	0.620	0.758
SPW [32] (8 × 8)	26.76	22.48	15.92	21.13	0.875	0.748	0.442	0.663
LCP [33] (8 × 8)	26.96	22.59	19.24	22.56	0.878	0.763	0.606	0.734
APAP [2] (100 × 100)	27.96	24.39	20.21	23.79	0.901	0.837	0.682	0.794
AANAP [21] (100 × 100)	27.80	24.05	19.91	23.52	0.897	0.829	0.668	0.785
robust ELA [31] (100 × 100)	29.28	25.12	19.15	23.98	0.917	0.853	0.689	0.806
SPW [32] (100 × 100)	26.87	22.74	16.85	21.61	0.880	0.759	0.494	0.689
LCP [33] (100 × 100)	26.43	22.53	19.28	22.40	0.873	0.760	0.611	0.734
Ours (8 × 8)	29.52	25.24	21.20	24.89	0.923	0.859	0.708	0.817



Fig. 8. Qualitative comparison with the state-of-the-arts on real-world dataset (UDIS-D). For each instance, we magnify a far region in a red box and a near region in a blue box to compare the alignment performance in scenes with parallax. The mesh-based methods adopt different mesh sizes because they reach the best performance at that size. (The details can be found in Table III(b) and Table VI.)

solutions can only work at a fixed resolution (128×128) due to the existence of fully connected layers. Following [20], we evaluate the performance using PSNR and SSIM in the overlapping regions, which can be calculated as follows:

$$\begin{aligned} PSNR_{overlap} &= PSNR(\mathcal{W}(E) \odot I_r, \mathcal{W}(I_t)), \\ SSIM_{overlap} &= SSIM(\mathcal{W}(E) \odot I_r, \mathcal{W}(I_t)), \end{aligned} \quad (11)$$

where $PSNR(\cdot)$ and $SSIM(\cdot)$ denote the operations of computing PSNR and SSIM between two images, respectively.

Form Table III, we can observe that:

(1) Our method is better than all the homography estimation methods in each case (“easy”, “moderate” and “hard”) of

different resolutions (128×128 and 512×512).

(2) The performance of the traditional solutions dorp as the resolution decreases because the performance of feature detection degrades in the low-resolution scenes.

(3) Most learning-based homography solutions do not work well because the overlap rates between the image pairs in this dataset are low. The long-range correlation can not be effectively learned by the convolutional layers or cost volume.

(4) The latest traditional multi-homography solutions (SPW and LCP) show unsatisfying performance in UDIS-D. The main reason is that they introduce other constraints except for the point-line alignment term such as distortion term and

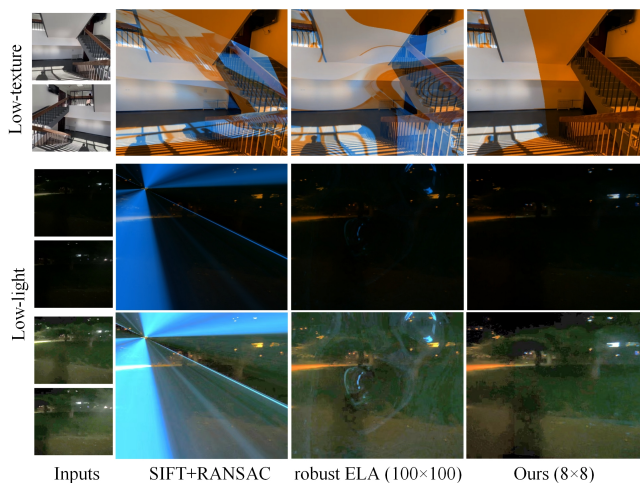


Fig. 9. Robust analysis on challenging cases. Row 1: A low-texture scene. Row 2-3: A low-light scene. The example in Row 2 is too challenging that we apply image augmentation on them, and the augmented results are demonstrated in Row 3.

line preserving term, reducing projective distortions at the cost of sacrificing alignment performance. Meanwhile, the point-line alignment could not work well in every scene, especially where the matched points and lines are not sufficient.

Qualitative Comparison.

In addition to Table III, we also provide a qualitative comparison between these methods in the original resolution of this real-world dataset. We choose the combination of SIFT and RANSAC as the representative work of traditional single homography solutions since it achieves the best alignment performance in UDIS-D. Also, LB-UDHN is chosen as the representative work of deep learning-based solutions for the best performance. To apply it to images with higher resolution (512×512), we multiply the estimated homography matrix by a scale transformation matrix to adapt to other resolutions. As for multi-homography solutions, we demonstrate their results with the mesh sets to 100×100 . Eight instances are displayed in Fig. 8, where each instance contains varying degrees of parallax. We fuse the reference image and the warped target image by setting the intensity of the blue channel in the reference image and that of the red channel in the warped target image to zero. In this manner, the non-overlapping regions are shown in orange, and the misalignments in the overlapping regions are highlighted in a different color. Although the proposed method cannot remove all the misalignments, the remaining misalignments in our results are less than that of other methods.

Robustness Analysis.

A robust method does not necessarily require good average performance (see ‘average’ columns of Table III) but requires that the worst performance cannot be poor (see ‘hard’ columns of Table III). Comparing Table III(a) with Table III(b), the performance of traditional solutions in high-resolution is significantly better because the feature points are more abundant when the resolution is increased.

However, for some challenging scenes such as low-light or low-texture, the increase in resolution does not improve the

performance. Fig. 9 demonstrates two challenging examples. When the texture is missing or the light is too low in a scene, the manual designed feature descriptors, *e.g.* SIFT, ORB and *etc.*, are not applicable, resulting in few feature points or mismatched feature correspondences. Compared with them, the deep learning solutions extract the feature maps by learning the distribution of dataset samples adaptively. Hence, the learning solutions are more robust.

Cross-dataset Validation.

For most deep learning methods, generalization is a flaw. In this section, we validate the generalization ability of the proposed method across datasets. Specifically, we train our network in UDIS-D and test it in other datasets. We collect the datasets from classic image stitching papers [2], [39]–[42], where these datasets are captured from different scenes and contain various degrees of parallax. The results are shown in Fig. 10. Even if it is tested on other datasets, our solution still has good alignment capabilities. Especially the overlap rates between input images in these examples are pretty low and most deep learning solutions could fail in these scenes.

D. Compared with Cost Volume

In addition to image alignment performance, we also compare the proposed CCL with the cost volume in the field of homography estimation. Both CCL and cost volume are modules used to extract matching information between feature correspondences without learning parameters. Both of them can easily be plugged into a neural network.

At first, we replaced the CCL with the cost volume in our network. Nevertheless, this replacement will bring about a dramatic increase in the number of network parameters, causing the training crash by exceeding the maximum memory of the GPU. Therefore, we design a relatively simple network as the baseline and compare the proposed CCL with the cost volume on this framework. The baseline architecture is shown in Fig. 11, where 8 convolutional layers with shared parameters and 3 max-pooling layers are adopted to extract the deep features. Then the matching information can be obtained from the feature maps extracted from different input images using a certain approach. Specifically, directly concatenating two convolutional layers with filter number setting to 256, the cost volume with search radius setting to 16, and the proposed CCL are adopted in different experiments. After that, we use three fully connected layers to predict the 8 motions of the 4 vertices in the target image.

The experiments are conducted on Warped MS-COCO in one RTX NVIDIA 2080 Ti and all the schemes are trained in a supervised manner for 80 epochs. The results are shown in Table IV, where a comprehensive evaluation of the performance, the number of parameters, and the speed is formulated. From this table, we can observe:

- (1) The performance of “Concatenation” is almost equal to $I_{3 \times 3}$ (18.5220, as shown in Table II). Without the matching relationship between the input feature maps, the network learns nothing.
- (2) The performance of “Convolution” is almost the same as that of “Concatenation”, which indicates convolutional layers

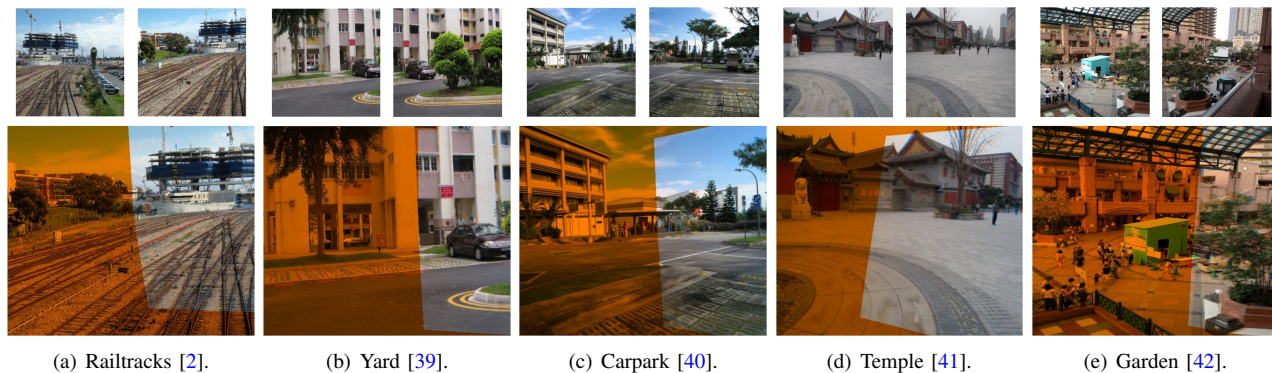


Fig. 10. Cross-dataset validation on generalization ability. Top to bottom: inputs and our aligned results.

TABLE IV

COMPREHENSIVE COMPARISON OF THE PERFORMANCE, THE NUMBER OF PARAMETERS, AND THE SPEED BETWEEN THE COST VOLUME AND PROPOSED CCL ON WARPED MS-COCO.

	Performance (\downarrow) (4-pt homography RMSE)	Model size (\downarrow) (/MB)	Time per iteration (\downarrow) (/ms)
Concatenation	18.5218	199.58	6.3500
Convolution	18.5218	213.08	6.6372
Cost Volume	14.0783	824.33	40.0687
CCL	4.7752	9.08	6.9576

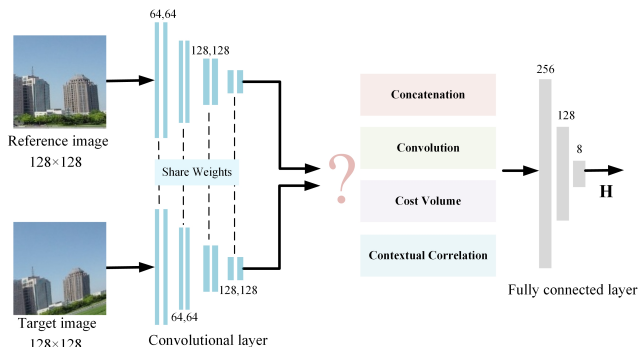


Fig. 11. The network architecture of the deep homography baseline in Section IV-D.

learn nothing about the matching relationship. The limited receptive field can interpret this phenomenon.

(3) The cost volume does help to extract the matching relationship between the input feature maps, but it is not efficient. Besides, the costs on parameters and speed are significantly increased.

(4) The performance of the proposed CCL is much better than that of the cost volume. In addition, this efficient module only increases 0.32ms running time compared with ‘‘Convolution’’. As for the model size, our design significantly decreases the parameters from several hundred MB to 10 MB.

Actually, the decrease in the model size mainly owes to the feature flow. This lightweight representation of feature correlation ($H \times W \times 2$) significantly reduces the parameters of the subsequent fully connected layer. Compared with the cost volume, the feature flow also rejects extensive redundant matching information, leading to more efficient prediction on homography.

TABLE V

ABLATION STUDIES OF CONTEXTUAL CORRELATION ON WARPED MS-COCO.

Correlation Volume	<input checked="" type="checkbox"/>	<input checked="" type="checkbox"/>	<input checked="" type="checkbox"/>
Scale Softmax			<input checked="" type="checkbox"/>
Feature Flow		<input checked="" type="checkbox"/>	<input checked="" type="checkbox"/>
Performance (\downarrow) (4-pt homography RMSE)	18.5218	6.6469	4.7752
Model size (\downarrow) (/MB)	199.58	9.08	9.08
Time per iteration (\downarrow) (/ms)	7.2594	6.9534	6.9576

TABLE VI

ABLATION STUDIES OF THE NUMBER OF GRIDS AND DEPTH-AWARE SHAPE-PRESERVED LOSS ON UDIS-D.

Multi-Grid	Depth-Aware SPL	Average PSNR (\uparrow)	Average SSIM (\uparrow)
1x1	<input checked="" type="checkbox"/>	23.1144	0.7541
2x2	<input checked="" type="checkbox"/>	23.1885	0.7598
4x4	<input checked="" type="checkbox"/>	24.6234	0.8093
8x8	<input checked="" type="checkbox"/>	24.7581	0.8129
16x16	<input checked="" type="checkbox"/>	24.6360	0.8086
8x8	1 depth levels	24.7124	0.8105
8x8	2 depth levels	24.7262	0.8113
8x8	4 depth levels	24.7669	0.8134
8x8	8 depth levels	24.8145	0.8146
8x8	16 depth levels	24.8622	0.8164
8x8	32 depth levels	24.8917	0.8174
8x8	48 depth levels	24.8707	0.8165

E. Ablation studies

Contextual Correlation. The CCL can be implemented in three steps and we carry on ablation experiments on these steps. We validate the effectiveness of every stage using the baseline network (shown in Fig. 11) on Warped MS-COCO, and the results are shown in Table V. ‘‘Feature Flow’’ can convert correlation volume into a simple but efficient represen-

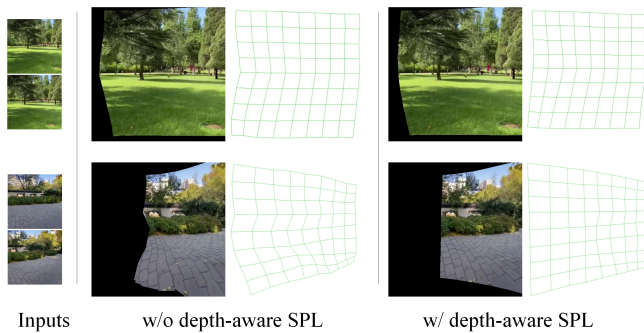


Fig. 12. Qualitative comparison on the mesh shape. The warped target image and the deformed mesh are shown in pair.

tation. And “Scale Softmax” can further improve the matching performance by effectively suppressing the interference of points with low matching probability on feature flow.

Number of Grids. The increase of the grids’ number can bring about an improvement in image alignment. But it is not absolute since the network architecture and the size of the dataset may affect it. Therefore, we explore the best number of grids in our work and the results are shown in Row 2-6 of Table VI. According to our experiment, 8×8 mesh is the best.

Depth-Aware Shape-Preserved Loss. The shape-preserved constraint can maintain the rigid shape of the mesh. But it regards all the grids as being on the same plane, reducing the alignment performance of the network in the existence of parallax. Dividing an image mesh into different depth levels can avoid this problem. We explore the best number of depth levels in our network, and the results are shown in Row 5, 7-13 of Table VI, where Row 5 can be regarded as no shape-preserved constraint and Row 7 can be considered as a global shape-preserved constraint (as [26], [34] do). Also, a qualitative comparison of the mesh shape is provided in Fig. 12 to demonstrate the superiority of our depth-aware shape-preserved loss.

V. CONCLUSION AND FUTURE PROSPECT

In this paper, we have proposed a depth-aware multi-grid deep homography estimation network to align images with parallax from global to local, breaking through the limitation of the existing single deep homography estimation solutions. In our network, we design the CCL to extract the matching relationship efficiently, outperforming the cost volume in performance, the number of parameters, and the speed. Besides, a depth-aware shape-preserved loss is presented to improve the shape regularity and alignment performance, simultaneously. Extensive experiments prove our superiority to the existing single homography and multi-homography solutions.

However, the number of grids can be limited by the network architecture and the size of the dataset. In the future, we would like to explore the reason that affects the number of grids and increase the upper limit of grids’ number without decreasing alignment performance.

REFERENCES

- [1] L. Nie, C. Lin, K. Liao, M. Liu, and Y. Zhao, “A view-free image stitching network based on global homography,” *Journal of Visual Communication and Image Representation*, p. 102950, 2020.
- [2] J. Zaragoza, T.-J. Chin, M. S. Brown, and D. Suter, “As-projective-as-possible image stitching with moving dlt,” in *Proceedings of the IEEE conference on computer vision and pattern recognition*, pp. 2339–2346, 2013.
- [3] L. Zhang, Q.-K. Xu, and H. Huang, “A global approach to fast video stabilization,” *IEEE Transactions on Circuits and Systems for Video Technology*, vol. 27, no. 2, pp. 225–235, 2017.
- [4] M. Zhao and Q. Ling, “Adaptively meshed video stabilization,” *IEEE Transactions on Circuits and Systems for Video Technology*, pp. 1–1, 2020.
- [5] S. Liu, P. Tan, L. Yuan, J. Sun, and B. Zeng, “Meshflow: Minimum latency online video stabilization,” in *European Conference on Computer Vision*, pp. 800–815, Springer, 2016.
- [6] Z. Zhang, “A flexible new technique for camera calibration,” *IEEE Transactions on pattern analysis and machine intelligence*, vol. 22, no. 11, pp. 1330–1334, 2000.
- [7] J. Engel, T. Schöps, and D. Cremers, “Lsd-slam: Large-scale direct monocular slam,” in *European conference on computer vision*, pp. 834–849, Springer, 2014.
- [8] B. D. Lucas and T. Kanade, “An iterative image registration technique with an application to stereo vision,” in *Proceedings of the 7th International Joint Conference on Artificial Intelligence - Volume 2*, p. 674–679, Morgan Kaufmann Publishers Inc., 1981.
- [9] D. G. Lowe, “Distinctive image features from scale-invariant keypoints,” *International journal of computer vision*, vol. 60, no. 2, pp. 91–110, 2004.
- [10] E. Rublee, V. Rabaud, K. Konolige, and G. Bradski, “Orb: An efficient alternative to sift or surf,” in *2011 International conference on computer vision*, pp. 2564–2571, Ieee, 2011.
- [11] S. Leutenegger, M. Chli, and R. Y. Siegwart, “Brisk: Binary robust invariant scalable keypoints,” in *2011 International conference on computer vision*, pp. 2548–2555, Ieee, 2011.
- [12] Y. Tian, X. Yu, B. Fan, F. Wu, H. Heijnen, and V. Balntas, “Sosnet: Second order similarity regularization for local descriptor learning,” in *CVPR*, 2019.
- [13] M. A. Fischler and R. C. Bolles, “Random sample consensus: a paradigm for model fitting with applications to image analysis and automated cartography,” *Communications of the ACM*, vol. 24, no. 6, pp. 381–395, 1981.
- [14] D. Barath, J. Matas, and J. Nuskova, “Magsac: marginalizing sample consensus,” in *Proceedings of the IEEE Conference on Computer Vision and Pattern Recognition*, pp. 10197–10205, 2019.
- [15] D. Barath, J. Nuskova, M. Ivashechkin, and J. Matas, “MAGSAC++, a fast, reliable and accurate robust estimator,” in *Conference on Computer Vision and Pattern Recognition*, 2020.
- [16] D. DeTone, T. Malisiewicz, and A. Rabinovich, “Deep image homography estimation,” *arXiv preprint arXiv:1606.03798*, 2016.
- [17] T. Nguyen, S. W. Chen, S. S. Shivakumar, C. J. Taylor, and V. Kumar, “Unsupervised deep homography: A fast and robust homography estimation model,” *IEEE Robotics and Automation Letters*, vol. 3, no. 3, pp. 2346–2353, 2018.
- [18] J. Zhang, C. Wang, S. Liu, L. Jia, N. Ye, J. Wang, J. Zhou, and J. Sun, “Content-aware unsupervised deep homography estimation,” in *European Conference on Computer Vision*, pp. 653–669, Springer, 2020.
- [19] L. Nie, C. Lin, K. Liao, and Y. Zhao, “Learning edge-preserved image stitching from large-baseline deep homography,” *arXiv preprint arXiv:2012.06194*, 2020.
- [20] L. Nie, C. Lin, K. Liao, S. Liu, and Y. Zhao, “Unsupervised deep image stitching: Reconstructing stitched features to images,” *IEEE Transactions on Image Processing*, vol. 30, pp. 6184–6197, 2021.
- [21] C.-C. Lin, S. U. Pankanti, K. Natesan Ramamurthy, and A. Y. Aravkin, “Adaptive as-natural-as-possible image stitching,” in *Proceedings of the IEEE Conference on Computer Vision and Pattern Recognition*, pp. 1155–1163, 2015.
- [22] K.-Y. Lee and J.-Y. Sim, “Warping residual based image stitching for large parallax,” in *Proceedings of the IEEE/CVF Conference on Computer Vision and Pattern Recognition*, pp. 8198–8206, 2020.
- [23] W. Xue, W. Xie, Y. Zhang, and S. Chen, “Stable linear structures and seam measurements for parallax image stitching,” *IEEE Transactions on Circuits and Systems for Video Technology*, pp. 1–1, 2021.

- [24] A. Hosni, C. Rhemann, M. Bleyer, C. Rother, and M. Gelautz, "Fast cost-volume filtering for visual correspondence and beyond," *IEEE Transactions on Pattern Analysis and Machine Intelligence*, vol. 35, no. 2, pp. 504–511, 2012.
- [25] D. Sun, X. Yang, M.-Y. Liu, and J. Kautz, "Pwc-net: Cnns for optical flow using pyramid, warping, and cost volume," in *Proceedings of the IEEE Conference on Computer Vision and Pattern Recognition*, pp. 8934–8943, 2018.
- [26] M. Wang, G.-Y. Yang, J.-K. Lin, S.-H. Zhang, A. Shamir, S.-P. Lu, and S.-M. Hu, "Deep online video stabilization with multi-grid warping transformation learning," *IEEE Transactions on Image Processing*, vol. 28, no. 5, pp. 2283–2292, 2018.
- [27] F. Liu, M. Gleicher, H. Jin, and A. Agarwala, "Content-preserving warps for 3d video stabilization," in *ACM SIGGRAPH 2009 Papers, SIGGRAPH '09*, (New York, NY, USA), Association for Computing Machinery, 2009.
- [28] M. Jaderberg, K. Simonyan, A. Zisserman, *et al.*, "Spatial transformer networks," in *Advances in neural information processing systems*, pp. 2017–2025, 2015.
- [29] H. Le, F. Liu, S. Zhang, and A. Agarwala, "Deep homography estimation for dynamic scenes," in *Proceedings of the IEEE/CVF Conference on Computer Vision and Pattern Recognition*, pp. 7652–7661, 2020.
- [30] C.-H. Chang, C.-N. Chou, and E. Y. Chang, "Clkn: Cascaded lucas-kanade networks for image alignment," in *2017 IEEE Conference on Computer Vision and Pattern Recognition (CVPR)*, pp. 3777–3785, 2017.
- [31] J. Li, Z. Wang, S. Lai, Y. Zhai, and M. Zhang, "Parallax-tolerant image stitching based on robust elastic warping," *IEEE Transactions on Multimedia*, vol. 20, no. 7, pp. 1672–1687, 2017.
- [32] T. Liao and N. Li, "Single-perspective warps in natural image stitching," *IEEE Transactions on Image Processing*, vol. 29, pp. 724–735, 2020.
- [33] Q. Jia, Z. Li, X. Fan, H. Zhao, S. Teng, X. Ye, and L. J. Latecki, "Leveraging line-point consistency to preserve structures for wide parallax image stitching," in *Proceedings of the IEEE/CVF Conference on Computer Vision and Pattern Recognition*, pp. 12186–12195, 2021.
- [34] N. Ye, C. Wang, S. Liu, L. Jia, J. Wang, and Y. Cui, "Deepmeshflow: Content adaptive mesh deformation for robust image registration," *arXiv preprint arXiv:1912.05131*, 2019.
- [35] G. Hinton, O. Vinyals, and J. Dean, "Distilling the knowledge in a neural network," *arXiv preprint arXiv:1503.02531*, 2015.
- [36] K. Xian, J. Zhang, O. Wang, L. Mai, Z. Lin, and Z. Cao, "Structure-guided ranking loss for single image depth prediction," in *The IEEE/CVF Conference on Computer Vision and Pattern Recognition (CVPR)*, June 2020.
- [37] D. P. Kingma and J. Ba, "Adam: A method for stochastic optimization," *arXiv preprint arXiv:1412.6980*, 2014.
- [38] Y. Zhao, X. Huang, and Z. Zhang, "Deep lucas-kanade homography for multimodal image alignment," *arXiv preprint arXiv:2104.11693*, 2021.
- [39] J. Gao, Y. Li, T.-J. Chin, and M. S. Brown, "Seam-driven image stitching," in *Eurographics (Short Papers)*, pp. 45–48, 2013.
- [40] C.-H. Chang, Y. Sato, and Y.-Y. Chuang, "Shape-preserving half-projective warps for image stitching," in *Proceedings of the IEEE Conference on Computer Vision and Pattern Recognition*, pp. 3254–3261, 2014.
- [41] J. Gao, S. J. Kim, and M. S. Brown, "Constructing image panoramas using dual-homography warping," in *CVPR 2011*, pp. 49–56, IEEE, 2011.
- [42] J. Li, B. Deng, R. Tang, Z. Wang, and Y. Yan, "Local-adaptive image alignment based on triangular facet approximation," *IEEE Transactions on Image Processing*, vol. 29, pp. 2356–2369, 2019.